Models for the pedestal temperature at the edge of H-mode tokamak plasmas

T. Onjun, G. Bateman, and A. H. Kritz
Lehigh University Physics Department, 16 Memorial Drive East, Bethlehem, Pennsylvania 18015

G. Hammett
Princeton Plasma Physics Laboratory, Princeton University, Princeton, New Jersey 08540

Predictive models are developed for the temperature at the top at the edge of type 1 ELMy (edge localized mode) H-mode (high-confinement mode) plasmas. Theory-motivated models are used for the pedestal width and pressure gradient, while the pedestal density is obtained from experimental data in this study. The pedestal pressure gradient is assumed to be limited by the ballooning mode instability and is expressed in terms of the magnetic shear and geometrical factors. The effect of the bootstrap current, which reduces the magnetic shear in the steep pressure gradient region at the edge of the H-mode plasma, is included in the determination of the magnetic shear. Approaches for calculating the magnetic shear, combined with proposed models for the pedestal width, are used to determine the pedestal temperature. The computed pedestal temperatures are compared with more than 500 measured pedestal temperatures for type 1 ELMy H-mode discharges in four tokamaks. Some of the uncertainties in these results are discussed, and directions for future work to improve edge pedestal scalings are described. © *2002 American Institute of Physics.*
[DOI: 10.1063/1.1518474]

I. INTRODUCTION

Energy confinement in the high-confinement (H-mode) regime of tokamaks is strongly dependent on the temperature at the top of the pedestal that forms at the edge of H-mode plasmas. The H-mode temperature and density pedestal is produced by a transport barrier characterized by a narrow sharply defined region of steep temperature and density gradients. This pedestal is located near the last closed magnetic flux surface and typically extends over with a width of less than 5%–10% of the plasma minor radius. Since the height of the pedestal strongly influences the plasma performance in the H-mode operation, it is important to understand the physics that governs the H-mode pedestal. Moreover, the temperature at the top of the pedestal is one of the boundary conditions required in integrated predictive tokamak transport modeling simulations.

Previous experimental studies of pedestal scalings have found a range of results for the pedestal height and width in various tokamaks. Some studies have found a scaling consistent with a pedestal width that is linearly proportional to the gyro-radius[1–5] combined with a simple expression for the gradient limited by ballooning modes (neglecting the bootstrap and separatrix effects discussed below in Sec. IV). Some earlier work from the Joint European Torus (JET) reported a weaker scaling for the inferred pedestal width—with the pedestal width, Δ, scaling as $\Delta \propto R(\rho_\theta/R)^\nu$, with ν in the range of 1/2 to 2/3,[6] where R is the plasma major radius and ρ_θ is the poloidal ion gyro-radius. Note, the notation and units used in this paper are described in Table I. Some early papers from the Doublet III-D Tokamak (DIII-D) team indicated that it was hard to distinguish between Δ/R $\propto(\rho_\theta/R)^{2/3}$ and $\Delta/R \propto \beta_\theta^{1/2}$ (where β_θ is the plasma pressure normalized by the poloidal magnetic pressure), but later experiments with a pumped divertor were able to reduce the correlation between density and plasma current and supported a pedestal width scaling $\Delta/R \propto \beta_\theta^{1/2}$.[7] The analysis from DIII-D also indicates that the second-stable regime of the ballooning modes can be accessed because of the reduction in the magnetic shear caused by the bootstrap current, which dominates in the pedestal region.[7,8] Also, Sugihara has suggested that the bootstrap current may affect scaling of the pedestal pressure in the first stability region.[9] In our paper, the effect of the bootstrap current on the magnetic shear and the proximity of the separatrix are considered for six pedestal width models that are theory-motivated.

An expression for the H-mode pedestal temperature is developed in Sec. II. In Sec. III, the experimental data used in this study are discussed. In Sec. IV, six pedestal width scalings are used to develop expressions for the temperature at the top of pedestal. In Sec. V, there is a description of the method used to determine the maximum normalized pressure gradient from the ballooning mode limit. The effect of the bootstrap current on magnetic shear is included. In Sec. VI, the predictions of the pedestal temperature resulting from the used of these models are compared with pedestal temperature data. A simple statistical analysis is used to characterize the agreement of the predictions of each model with experimental data. The uncertainty of the results is discussed and a suggestion is made for a new experiment that might help to refine the pedestal model. In Sec. VII, conclusions are presented.

Phys. Plasmas, Vol. 9, No. 12, December 2002

Models for the pedestal temperature at the edge . . .   5019

TABLE I. Notation used in this paper.

a	m	plasma minor radius (half-width)
r	m	flux surface minor radius (half-width)
R	m	major radius to geometric center of each flux surface
κ		plasma elongation
δ		plasma triangularity
B_T	Tesla	vacuum toroidal magnetic field at R
I_p	MA	toroidal plasma current
n_{ped}	m^{-3}	pedestal density
n_{Gr}	m^{-3}	Greenwald density limit $[I/\pi a^2 10^{20}]$
E_r	V/m	radial electric field
T_{ped}	keV	pedestal temperature
A_H	AMU	average hydrogenic mass
k	J/K	Boltzmann constant
μ_0	Hm^{-1}	permeability of free space
c_s	m/s	sound speed $[(kT_e/m_i)^{1/2}]$
ω_{ci}	1/s	ion gyro-frequency $[eB_T/m_i]$
ρ	m	ion gyro-radius $[4.57\times10^{-3}\sqrt{A_H T[\mathrm{keV}]/B}]$
ρ_θ	m	poloidal ion gyro-radius
β_θ		normalized poloidal pressure
$\langle B_\theta \rangle$		average poloidal field around flux surface $(\approx \mu_0 I_p/(\pi a(1+\kappa)))$
Z_{eff}		measure of the impurity concentration
ν_e	1/s	electron collision frequency $[1.09\times10^{16}T_e^{3/2}/(Z_{\mathrm{eff}}^2 n \ln \Lambda_e)]^{-1}$
ν_i	1/s	ion collision frequency $[6.6\times10^{17}\sqrt{A_H}T_e^{3/2}/(Z_{\mathrm{eff}}^4 n \ln \Lambda_i)]^{-1}$
ω_{bj}	1/s	trapped particle bounce frequency $[\epsilon^{1/2}(T_j/m_j)^{1/2}/Rq]$

II. H-MODE PEDESTAL TEMPERATURE

The pedestal region is illustrated in Fig. 1. If the pressure gradient ($\partial p/\partial r$) within the pedestal region is constant, the pressure at the top of pedestal (p_{ped}) is

$$p_{\mathrm{ped}} \equiv 2n_{\mathrm{ped}}kT_{\mathrm{ped}} = \Delta \left| \frac{\partial p}{\partial r} \right|, \tag{1}$$

where n_{ped} and T_{ped} are the density and temperature at the
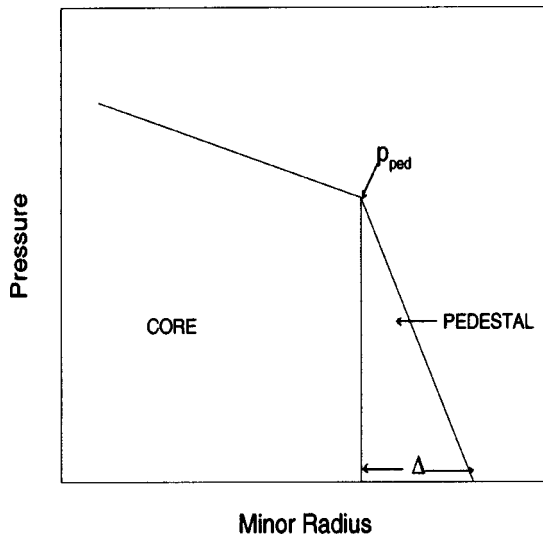
FIG. 1. Plot for the pressure profile near the edge of the H-mode plasmas. The H-mode edge pedestal is a region of steep gradient at the edge of plasma.

top of the pedestal, k is the Boltzmann's constant, and Δ is the pedestal width. Rewriting Eq. (1), one can obtain the value of T_{ped}

$$T_{\mathrm{ped}} = \frac{1}{2kn_{\mathrm{ped}}} \Delta \left| \frac{\partial p}{\partial r} \right|, \tag{2}$$

given the value of the pressure gradient in the pedestal region and the width of the pedestal region. (The pedestal density is obtained from experimental data, in this study.) The focus of this paper is to examine models for estimating the pedestal pressure gradient and pedestal width. These models are evaluated by comparing the resulting predictions for T_{ped} with corresponding experimental data.

In determining the pressure gradient inside the pedestal region for the type 1 ELMy H-mode discharges,[10] it is assumed that the pressure gradient is limited by the ballooning mode instability. Recognizing that the pressure gradient in the pedestal region may depend on parameters such as magnetic shear (s), elongation (κ), and triangularity (δ), we define the maximum normalized pressure gradient that is the critical pressure gradient, α_c, as

$$\alpha_c \equiv -\frac{2\mu_0 R q^2}{B_T^2}\left(\frac{\partial p}{\partial r}\right)_c = \alpha_c(s,\kappa,\delta). \tag{3}$$

The temperature at the top of pedestal can then be computed in terms of α_c using the equation

$$T_{\mathrm{ped}} = \frac{\Delta}{2kn_{\mathrm{ped}}} \frac{\alpha_c B_T^2}{2\mu_0 R q^2}. \tag{4}$$

5020   Phys. Plasmas, Vol. 9, No. 12, December 2002

Onjun *et al.*

If the maximum normalized pressure gradient, α_c, and the pedestal width, Δ, are determined, Eq. (4) can be used to obtain the temperature at the top of the pedestal.

In this paper, the time-dependent effects of edge localized modes (ELMs) are not considered. Consequently, the evaluation of the pedestal temperature is taken to be the temperature prior to the occurrence of each ELM. The plasma ions are assumed to be primarily hydrogenic. The only effect of the impurity concentration is through the calculation of the plasma collisionality, which affects the bootstrap current. Also, it is assumed that the electron and ion temperatures are equal.

In general, the pedestal density is more constrained than the pedestal temperature. That is, the density profile between the pedestal and the magnetic axis is usually rather flat in H-mode discharges, so that the pedestal density is a large fraction of the line average density. Hence, the focus of this paper is on developing a model for the pedestal temperature rather than for the density. Measured values of the pedestal density are used in Eq. (4).

III. EXPERIMENTAL DATA

The experimental data used in this study are taken from the International Pedestal Database.[11] The International Pedestal Database currently contains data from five tokamaks, the Alcator C-Mod tokamak (C-Mod),[12] the Axially Symmetric Divertor Experiment (ASDEX-U),[13] DIII-D,[14] the Joint European Torus tokamak (JET),[15] and the upgraded Japan Atomic Energy Research Institute Tokamak-60 (JT-60U).[16] In this study, we use data from the current public version of the INTERNATIONAL PEDESTAL DATABASE (version 3.1), for type 1 ELMy H-mode discharges. As a result, 533 data points are used in this study—367 JT-60U, 105 ASDEX-U, 56 JET, and 5 DIII-D. Different approaches are used to identify the location of the top of pedestal in each machine. For the ASDEX-U discharges, the top of pedestal is defined as located a distance of 2 cm away from the separatrix. A tanh fit method is used to locate the top of the pedestal in the DIII-D discharges while a linear fit method is applied for the JET discharges. For the JT-60U discharges, the location of the top of the pedestal is defined as located at the 95% flux surface. When the experimental ion pedestal temperatures ($T_{i,ped}$) are available, they are used to calibrate the models. When ion temperatures are not available, the experimental electron temperatures ($T_{e,ped}$) are used.

To quantify the comparison between the predictions of each model and experimental data, the root mean-square error (RMSE) is computed. The RMSE is defined as

$$\text{RMSE}(\%) \equiv \sqrt{\frac{1}{N-1} \sum_{j=1}^{N} (\ln(T_{\exp_j}) - \ln(T_{\text{mod}_j}))^2}$$

$$\times 100, \tag{5}$$

and the offset, as

$$\text{Offset} \equiv \frac{1}{N} \sum_{j=1}^{N} (\ln(T_{\exp_j}) - \ln(T_{\text{mod}_j})), \tag{6}$$

where N is total number of data points, and $T_{\exp_j}$ and $T_{\exp_j}$ are the jth experimental and model results for the temperature.

IV. SCALING OF PEDESTAL WIDTH

In this paper, six theory motivated models for the pedestal width are applied in determining the pedestal temperatures that are compared with experimental data.

A. Width scaling 1—based on magnetic and flow shear stabilization

The basic assumption of this model is that the transport barrier is formed in the region where the turbulence growth rate is balanced by a stabilizing $\mathbf{E_r} \times \mathbf{B}$ shearing rate. In the pedestal of a well developed H-mode, it is assumed that the radial electric field, E_r, is produced by the pressure gradient, $\partial p / \partial r$, so that

$$neE_r = \frac{\partial p}{\partial r}, \tag{7}$$

where n is the plasma density and e is the electron charge. This results in the $\mathbf{E_r} \times \mathbf{B}$ drift velocity given by

$$v_{\mathbf{E_r} \times \mathbf{B}} = \frac{E_r}{B_T} = \frac{1}{neB_T} \frac{\partial p}{\partial r} \approx \frac{1}{neB_T} \frac{p}{\Delta} \approx \frac{\rho c_s}{\Delta}, \tag{8}$$

where ρ is the ion gyro radius and c_s is the ion sound velocity. The resulting shearing rate, $\gamma_{\mathbf{E_r} \times \mathbf{B}}$, is

$$\gamma_{\mathbf{E_r} \times \mathbf{B}} = \frac{\partial v_{\mathbf{E_r} \times \mathbf{B}}}{\partial r} \approx \frac{\rho c_s}{\Delta^2}. \tag{9}$$

In this model, it is assumed that the turbulence that drives transport with gyro-Bohm scaling is stabilized by the magnetic and flow shear in the pedestal region.[9] In particular, it is assumed that the maximum growth rate, for the instability associated with this drift wave turbulence, scales as

$$\gamma_{\text{max}} \propto \frac{c_s}{\Delta} \frac{1}{s^2}, \tag{10}$$

where s is the magnetic shear. The turbulence is suppressed when the $\mathbf{E_r} \times \mathbf{B}$ shearing rate is equal to or larger than the maximum growth rate

$$\gamma_{\mathbf{E_r} \times \mathbf{B}} \geq \gamma_{\text{max}}. \tag{11}$$

By equating Eqs. (9) and (10) (using a constant of proportionality, C_1), the scaling of the pedestal width is found to be

$$\Delta = C_1 \rho s^2 = C_1 \left(4.57 \times 10^{-3} \frac{\sqrt{A_H T_{\text{ped}}}}{B_T} \right) s^2, \tag{12}$$

where A_H is the average hydrogenic mass. By using this scaling for the pedestal width in Eq. (4), the temperature at the top of pedestal can be obtained from

$$T_{\text{ped}} = C_1^2 \left(\left(\frac{4.57 \times 10^{-3}}{4\mu_0 (1.6022 \times 10^{-16})} \right)^2 \left(\frac{B_T^2}{q^4} \right) \left(\frac{A_H}{R^2} \right) \right.$$

$$\left. \times \left(\frac{\alpha_c}{n_{\text{ped}}} \right)^2 s^4 \right), \tag{13}$$

where C_1 is the constant of proportionality in Eq. (12). The constant C_1 is chosen so as to optimize the agreement between the measured values of T_{ped} and the model results for T_{ped} by minimizing the RMSE. Equation (13) contains T_{ped} on both the left and right sides and is nonlinear in T_{ped} since q, α_c, and s are functions of position in the pedestal and, as a result, nonlinear functions of T_{ped}. An iterative procedure is used in this paper to determine the temperature at the top of the pedestal.

B. Width scaling 2—based on flow shear stabilization

In this model, the $\mathbf{E}_r \times \mathbf{B}$ suppression of long wavelength modes is assumed to be the relevant factor in establishing the edge transport barrier. The local growth of the long wavelength modes, γ_{local}, can be estimated by sound speed, c_s, divided by the connection length between the bad curvature region, the destabilizing curvature region on the outer side of the torus, and the good curvature region, the stabilizing curvature region on the inner side of the torus, in the pedestal region. The resulting growth rate is given by

$$\gamma_{local} \sim \frac{c_s}{qR}, \tag{14}$$

where R is the major radius and q is the safety factor. It is assumed that the turbulence is suppressed when the $\mathbf{E}_r \times \mathbf{B}$ shearing rate is larger than the local growth rate, that is when

$$\gamma_{\mathbf{E}_r \times \mathbf{B}} \gtrsim \gamma_{local}. \tag{15}$$

With the use of Eqs. (9), (14), and (15), the following result for the pedestal width is obtained

$$\Delta = C_2 \sqrt{\rho R q}. \tag{16}$$

By combining Eqs. (4) and (16), the temperature at the top of the pedestal can be obtained from the nonlinear equation (which again contains T_{ped} on both left and right sides)

$$T_{ped} = C_2^{4/3} \left(\left(\frac{(4.57 \times 10^{-3})^{1/2}}{4 \mu_0 (1.6022 \times 10^{-16})} \right)^{4/3} \left(\frac{B_T}{q} \right)^2 \right.$$
$$\left. \times \left(\frac{\sqrt{A_H}}{R} \right)^{2/3} \left(\frac{\alpha_c}{n_{ped}} \right)^{4/3} \right), \tag{17}$$

where C_2 is the constant of proportionality in Eq. (16).

C. Width scaling 3—based on diamagnetic stabilization

For this model, the ideal ballooning mode growth rate is approximated by $\gamma_b \approx [2c_s^2/(L_p R)]^{1/2}$, where $L_p \equiv -p/(dp/dr)$ is the pressure gradient scale length.[17] It is assumed that the pedestal width, Δ, is approximately equal to V_{*i}/γ_b where V_{*i}, the ion diamagnetic velocity, equals $\rho^2 \omega_{ci}/L_{pi}$. It is also assumed that the ion pressure gradient scale length, L_{pi}, and total pressure gradient scale length, L_p, are both approximately equal to the width of the pedestal, $L_p \sim L_{pi} \sim \Delta$. It then follows that the pedestal width scales as

$$\Delta = C_3 \rho^{2/3} R^{1/3}. \tag{18}$$

By using Eqs. (4) and (18), the temperature at the top of pedestal can be calculated from the nonlinear equation (with T_{ped} appearing explicitly on the left side and implicitly on the right side)

$$T_{ped} = C_3^{3/2} \left(\left(\frac{(4.57 \times 10^{-3})^{2/3}}{4 \mu_0 (1.6022 \times 10^{-16})} \right)^{3/2} \left(\frac{B_T^2}{q^3} \right) \left(\frac{\sqrt{A_H}}{R} \right) \right.$$
$$\left. \times \left(\frac{\alpha_c}{n_{ped}} \right)^{3/2} \right). \tag{19}$$

D. Width scaling 4—based on neutral penetration

Neutral particles, which usually come from the scrape of layer region, are believed to affect the dynamics of the H-mode, especially the formation of the H-mode pedestal. The neutrals can penetrate inside separatrix and affect the H-mode by modifying the particle, momentum, and energy balance of the main plasma. Penetration of neutral particles into plasma core is mainly controlled by the charge-exchange collisions with main ions and ionization of neutrals by a nonelastic collisions with electrons. Since the charge-exchange is a random-walk process, and the charge-exchange rate is usually much larger than the ionization rate, the migration of neutrals from outside plasmas can be considered as the diffusion process, with a random walk of step size $\lambda_{cx} = v_i / n_i \langle \sigma_{cx} v_i \rangle$ and frequency of steps $\nu_{cx} = n_i \langle \sigma_{cx} v_i \rangle$, where σ_{cx} is the charge exchange cross section. The resulting diffusion coefficient from the charge exchange is

$$D \approx \lambda_{cx}^2 \nu_{cx} \approx \frac{v_i^2}{n_i \langle \sigma_{cx} v_i \rangle}. \tag{20}$$

The diffusion equation for the steady-state neutral density, N, with the effect of ionization included can be written as

$$D \frac{\partial^2 N}{\partial x^2} = n_e N \langle \sigma_{ion} v_e \rangle, \tag{21}$$

where $v_e = \sqrt{2kT_e/m_e}$ is the electron thermal velocity. The equations above can lead to the estimation of the penetration length as

$$\Delta x \approx \sqrt{\frac{v_i^2}{n_i^2 \langle \sigma_{cx} v_i \rangle \langle \sigma_{ion} v_e \rangle}}. \tag{22}$$

In this model, the width of the barrier is assumed to be the length that neutral particles penetrate into the plasma. For simplicity, it is assumed that pressure at the top of the barrier is constant, which results in $v_i \propto \sqrt{T_i} \propto \sqrt{1/n_i}$, and $\langle \sigma_{cx} v_i \rangle$ and $\langle \sigma_{ion} v_e \rangle$ are independent of pedestal temperature. The resulting width of the pedestal scales inversely proportional to the pedestal density, that is

$$\Delta = C_4 \frac{1 \times 10^{27}}{n_{ped}^{3/2}}, \tag{23}$$

where $n_{ped} = n_i$ is the pedestal density. By using Eqs. (4) and (23), the temperature at the top of pedestal is obtained from the nonlinear equation

$$T_{\text{ped}}= C_4\left(\left(\frac{1\times10^{27}}{4\mu_0(1.6022\times10^{-16})}\right)\left(\frac{B_T}{q}\right)^2\left(\frac{1}{R}\right)\left(\frac{\alpha_c}{n_{\text{ped}}^{5/2}}\right)\right),$$
(24)

where T_{ped} appears implicitly on the right side.

E. Width scaling 5—based on ion orbit loss

In Shaing's model[18] based on ion orbit loss, the predicted width of the pedestal is

$$\Delta\propto\sqrt{\epsilon}\frac{\rho_\theta}{\sqrt{s_{\text{orbit}}}},$$
(25)

where ρ_θ is the ion poloidal gyro radius and s_{orbit} is a term due to squeezing of the banana orbits by the radial electric field. If it is assumed that s_{orbit} is constant, then the scaling of the pedestal width is

$$\Delta=C_5\sqrt{\epsilon}\rho_\theta\approx C_5\epsilon^{-1/2}q\rho/\kappa_{95},$$
(26)

where ϵ is the aspect ratio, a/R and where κ_{95} is elongation at the 95% flux surface and is taken to be 0.914 times the the value of the elongation at the separatrix. By using Eqs. (4) and (26), the temperature at the top of pedestal is obtained iteratively from the nonlinear equation where again T_{ped} appears both on the left side and implicitly on the right side

$$T_{\text{ped}}= C_5^2\left(\left(\frac{(4.57\times10^{-3})}{4\mu_0(1.6022\times10^{-16})}\right)^2\left(\frac{B_T}{q}\right)^2\left(\frac{A_H}{\kappa_{95}^2aR}\right)\right.$$
$$\left.\times\left(\frac{\alpha_c}{n_{\text{ped}}}\right)^2\right),$$
(27)

where C_5 is the constant of proportionality in Eq. (26).

F. Width scaling 6—based on normalized poloidal pressure

In this model, the scaling of pedestal width is based on a model proposed by Osborne:[7]

$$\Delta=C_6\sqrt{\beta_\theta}\ R=C_6\sqrt{\frac{4\mu_0n_{\text{ped}}kT_{\text{ped}}}{\langle B_\theta\rangle^2}}R,$$
(28)

where β_θ is the normalized poloidal pressure and $\langle B_\theta\rangle$ is the average poloidal field around the flux surface. By using Eqs. (4) and (28), the temperature at the top of pedestal can be obtained from the nonlinear equation

$$T_{\text{ped}}=C_6^2\left(\left(\frac{1}{4\mu_0(1.6022\times10^{-16})}\right)\left(\frac{B_T}{q^2}\right)^2\left(\frac{R}{a}\right)^2\left(\frac{\alpha_c^2}{n_{\text{ped}}}\right)\right.$$
$$\left.\times\left(\frac{\pi q_{95}(1+\kappa_{95})}{5g_s}\right)^2\right),$$
(29)

where C_6 is the constant of proportionality in Eq. (28) and q_{95}, the safety factor at the 95% flux surface, with geometrical effects included, is defined by

$$q_{95}=\frac{5a^2B_T}{\mu_0I_pR}g_s(\kappa_{95},\delta_{95},\epsilon),$$
(30)

and where the geometrical factor, g_s, is taken to be

$$g_s(\kappa_{95},\delta_{95},\epsilon)$$
$$=\frac{[1+\kappa_{95}^2(1+2\delta_{95}^2-1.2\delta_{95}^3)](1.17-0.65\epsilon)}{2(1-\epsilon^2)^2},$$
(31)

which is similar to Uckan's approximate fit to numerical equilibria[19] expressing the safety factor q_{95} in terms of the magnetic field, plasma current, and shaping effects such as elongation κ_{95}, triangularity δ_{95} (assumed to be approximately 0.85 times the value of triangularity at the separatrix) and aspect ratio $\epsilon=a/r$.

V. SCALING OF MAXIMUM NORMALIZED PRESSURE GRADIENT

The pressure gradient in the pedestal region is assumed, in this paper, to be limited by high-n ballooning modes[20] in the short toroidal wavelength limit. Ballooning stability is usually studied in terms of the $s-\alpha$ diagram. At high magnetic shear, the first stability boundary in the large aspect-ratio circular limit is given by

$$\alpha_c\approx0.8s,$$
(32)

where the magnetic shear is $s=(r/q)\partial q/\partial r$. There are limited analytic and numerical studies of global beta limits for noncircular plasmas. It is these studies that yield a plasma shape dependence of α_c, such as those used in Ref. 21. To roughly approximate the effect of plasma shape, one might modify the local ballooning limit to include a shaping factor, for example,

$$\alpha_c=0.8\,sf_s(\kappa,\delta,\epsilon).$$
(33)

One possible approximation for the shaping factor is to assume that f_s is given by the expression for g_s in Eq. (31). The form for g_s is suggested by the Troyon beta limit, which is based on numerical studies of a range of tokamak equilibria. In those studies, averages are taken over all flux surfaces, many of which have limited dependence on triangularity. The local pressure gradient limit is likely to be more strongly dependent on triangularity than that of the shaping factor in the global average pressure limit, g_s, in Eq. (31). There is empirical evidence for this in studies of the well-known favorable effects of high triangularity on confinement in tokamaks such as JT-60 and DIII-D. For example, a rough fit to the measurements in Refs. 3 and 4 suggests the dependence of α_c on triangularity could be as strong as $\alpha_c\propto(1+10\delta^2)$. In this paper, we will use a slightly more conservative scaling for the plasma shape dependence, namely,

$$\alpha_c=0.8s\,\frac{1+\kappa_{95}^2(1+5\delta_{95}^2)}{2}.$$
(34)

The effect of bootstrap current on ballooning stability is also include in this study. The bootstrap current, which is driven by the strong pressure gradient in the pedestal region, reduces the magnetic shear in that region. The magnetic shear at the edge of the plasma, when the effect of the bootstrap current is included, can be approximated to first order, by

$$s \approx s_0 \left(1 - \frac{\pi r^2 j_b}{I_p} \right), \tag{35}$$

where s_0 is the value of magnetic shear in the absence of the bootstrap current. (The value of s_0 can be determined following one of the several approaches described below.) As described in Ref. 20, the bootstrap current can be approximated in terms of temperature and pressure gradients with respect to the poloidal flux, Ψ, and in terms of the trapped particle fraction ($\approx \sqrt{2\epsilon} = \sqrt{2a/R}$) by

$$\langle \mathbf{j}_b \cdot \mathbf{B}_T \rangle = \frac{p_e R B_T \sqrt{2\epsilon}}{D} \left(b_1 \frac{1}{p_e} \frac{dp_e}{d\Psi} + b_2 \frac{1}{p_i} \frac{dp_i}{d\Psi} \right.$$

$$\left. + b_3 \frac{1}{T_e} \frac{dT_e}{d\Psi} + b_4 \frac{1}{T_i} \frac{dT_i}{d\Psi} \right), \tag{36}$$

where

$$b_1 = \frac{4.0 + 2.6\sqrt{2\epsilon}}{(1.0 + 1.02\nu_{*e}^{0.5} + 1.07\nu_{*e})(1.0 + 1.07\epsilon^{1.5}\nu_{*e})},$$

$$b_2 = \frac{T_i}{T_e} b_1,$$

$$b_3 = \frac{7.0 + 6.5\sqrt{2\epsilon}}{(1.0 + 0.57\nu_{*e}^{0.5} + 0.61\nu_{*e})(1.0 + 0.61\epsilon^{1.5}\nu_{*e})}$$

$$- \frac{5}{2} b_1,$$

$$b_4 = \left(\frac{-1.17/(1 + 0.46\sqrt{2\epsilon}) + 0.35\nu_{*i}^{0.5}}{1.0 + 0.70\nu_{*i}^{0.5}} \right.$$

$$\left. + 2.10\nu_{*i}^2 \epsilon^3 \right) \frac{1}{(1.0 + \nu_{*i}^2 \epsilon^3)(1.0 + \nu_{*e}^2 \epsilon^3)} b_2,$$

$$D = 2.4 + 5.4\sqrt{2\epsilon} + 5.2\epsilon,$$

and ν_{*j} is the normalized collisionality of the particle type j. The quantity ν_{*j} is defined as

$$\nu_{*j} = \frac{\nu_j}{\epsilon \omega_{bj}},$$

where ν_j is the collision frequency and ω_{bj} is the trapped particle bounce frequency of particle type j, as defined in Table I.

With the assumptions that $T_i \approx T_e$ and $n_i \approx n_e$, that the density scale length in the pedestal region is the same as the temperature scale length, and that the bootstrap current is nearly in the toroidal direction, Eq. (36) can be simplified

$$j_b = \frac{R\sqrt{2\epsilon}}{2D} \left(b_1 + b_2 + \frac{b_3}{2} + \frac{b_4}{2} \right) \frac{dp}{d\Psi}.$$

The poloidal flux can be approximated

$$d\Psi = 2\pi R B_\theta dr,$$

so that the bootstrap current can be further simplified to

$$j_b = C_{bs} b(\nu_*, \epsilon) \left(\frac{\sqrt{\epsilon}}{B_\theta} \right) \frac{dp}{dr}, \tag{37}$$

where the multiplier C_{bs} has a default value of 1.0 (this value will be varied later to study uncertainties in the bootstrap current effect) and

$$b(\nu_*, \epsilon) = \frac{b_1 + b_2 + \frac{b_3}{2} + \frac{b_4}{2}}{2\sqrt{2}\pi D}.$$

The safety factor, q, can be approximated for circular plasma as

$$q \approx q_{\text{circular}} \equiv \frac{aB_T}{RB_\theta} \approx \frac{aB_T}{R\left(\frac{\mu_0 I_p}{2\pi a}\right)}. \tag{38}$$

By using Eqs. (3), (35), (37), and (38), the magnetic shear, including the effect of bootstrap current, can be written

$$s = s_0 \left(1 - \frac{C_{bs} b(\nu_*, \epsilon) \alpha_c}{4\sqrt{\epsilon}} \right). \tag{39}$$

The solution of Eqs. (34) and (39) yields the following results for the maximum normalized pressure gradient, α_c,

$$\alpha_c = \frac{0.4 s_0 (1 + \kappa_{95}^2 (1 + 5\delta_{95}^2)) h_s}{1 + \frac{0.1 s_0 C_{bs} b(\nu_*, \epsilon)(1 + \kappa_{95}^2 (1 + 5\delta_{95}^2))}{\sqrt{\epsilon}}}, \tag{40}$$

and for the magnetic shear, s,

$$s = \frac{s_0}{1 + \frac{0.1 s_0 C_{bs} b(\nu_*, \epsilon)(1 + \kappa_{95}^2 (1 + 5\delta_{95}^2))}{\sqrt{\epsilon}}}. \tag{41}$$

Note that the coefficient h_s in Eq. (40) is an empirical factor that has been included to explore possible additional dependence on the plasma shape. For most models, h_s is set to be 1.0, except in Table V where the effect of the addition shaping h_s is explored.

There remains the issue of the determination of s_0. There is the suggestion that the global magnetic shear and the safety factor may be functions of distance from the separatrix.[9] Note that the safety factor, q, has a logarithmic singularity near the separatrix, and both the magnetic shear and the safety factor are actually infinite at the separatrix. A prescription to address this issue has been proposed by Sugihara.[9] His prescription is to evaluate the magnetic shear and the safety factor, needed for ballooning stability, at one pedestal width away the separatrix. Using this approach, we approximate the safety factor near the separatrix by this expression

$$q(x) = \frac{q_{95}}{\left(1 + \left(\frac{0.95}{1.4}\right)^2\right)^2 + 0.267|\ln(1 - 0.95)|}$$

$$\times \left[\left(1 + \left(\frac{x}{1.4}\right)^2\right)^2 + 0.267|\ln(1 - x)| \right], \tag{42}$$

where x is the normalized coordinate evaluated one pedestal width from the separatrix

5024   Phys. Plasmas, Vol. 9, No. 12, December 2002

Onjun *et al.*

TABLE II. Coefficient and RMSE of the models using Sugihara's shear prescription for type 1 ELMy H-mode discharges.

Model	Width scaling	C_w	RMSE(%)
1a	$\Delta \propto \rho s^2$	2.42	32.0
2a	$\Delta \propto \sqrt{\rho R q}$	0.22	30.8
3a	$\Delta \propto \rho^{2/3} R^{1/3}$	1.32	33.7
4a	$\Delta \propto 1/n_{\mathrm{ped}}^{3/2}$	2.60	53.4
5a	$\Delta \propto \epsilon^{1/2} \rho_\theta$	2.57	34.4
6a	$\Delta \propto \sqrt{\beta_\theta} R$	0.021	32.9

$$x = 1 - \frac{\Delta}{a}, \tag{43}$$

and q_{95}, the safety factor at the 95% flux surface, with geometrical effects included.[19] Finally, s_0 is determined from

$$s_0 = \frac{x}{q} \frac{\partial q}{\partial x}, \tag{44}$$

where q is given by Eq. (42). Since the width of the pedestal involves ballooning stability, this leads to nonlinear equations for the pedestal temperature that are solved iteratively.

While this might appear to address the issue of how to compute s_0, the theoretical basis for utilizing global magnetic shear is uncertain. This uncertainty is because one might think that ballooning modes, which are localized in the bad curvature region, might be controlled by the local magnetic shear, which is proportional to $\partial B_\theta / \partial r$, and the local pitch of the magnetic field, B_θ / B_T. These quantities are perfectly finite and continuous across the separatrix in the bad curvature region even though the flux surface quantities of the magnetic shear and the safety factor, which have nonlocal definitions, have singularities there. This has been demonstrated for ballooning modes in model separatrix equilibria.[22] As a result, we also consider models in which the pedestal temperature is evaluated using the value of constant magnetic shear ($s_0 = 2$) and the value of the safety factor at the 95% flux surface ($q = q_{95}$) as representative values of the local magnetic pitch and local shear in the bad curvature region.

VI. DISCUSSION

A. Results

Table II summarizes the RMSE [Eq. (5)] that results when the set of six pedestal width models along with the Sugihara prescription for the edge magnetic shear, s, and the safety factor, q (that is computed a pedestal width away from the separatrix) are compared with the full database (all 533 data points with type 1 ELMs). The RMS errors in Table II range from 30.8% to 53.4%. The model in which the pedestal width is based on the flow shear stabilization (Model 2a) yields the lowest RMSE and the model in which the pedestal width is based on the neutral penetration (Model 4a) yields the highest RMSE. It is difficult to see a noticeable difference between the models in the plots that show the compari-
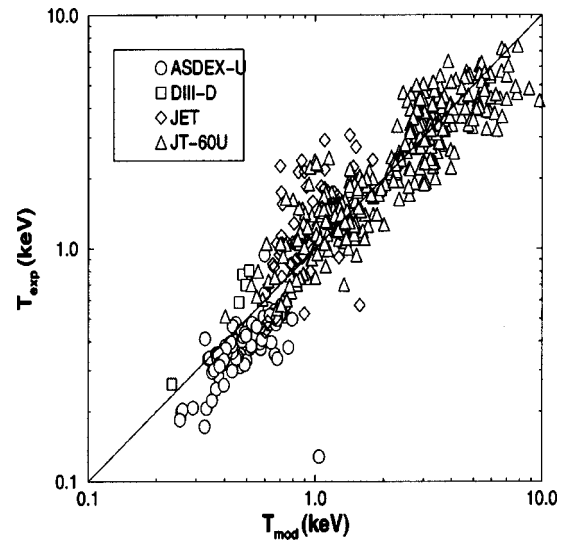
FIG. 2. Plot for the pedestal temperature predicted by Model 1a ($\Delta \propto \rho s^2$) compared with experimental data from 533 data points. Each tokamak is indicated by a different symbol.

son between the temperature predicted by these six models and experimental data, Figs. 2–7, except for the neutral penetration, Fig. 5, which has a worse fit.

It is worth noting that when Sugihara's shear prescription is used to calculate magnetic shear and safety factor for the ballooning instability, Eqs. (13), (17), (19), (24), (27), and (29), used to produce the results in Figs. 2–7, are nonlinear equations. Sugihara's shear prescription is to calculate the magnetic shear and the safety factor at a distance of one pedestal width away from separatrix. This leads to a nonlinear feedback mechanism which reduces the sensitivity of the predicted pedestal temperature to the assumed scaling of the pedestal width, since a narrower pedestal width will produce a higher magnetic shear and, thus, a steeper pressure gradient. In addition, the magnetic shear, s, is modified by the bootstrap current, which depends on collisionality, which is a
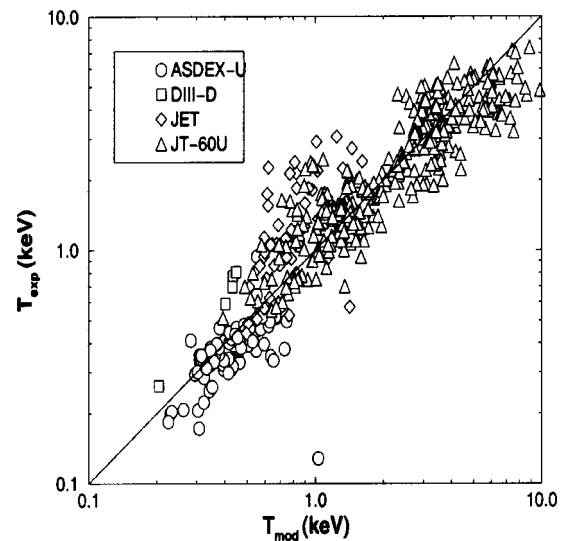
FIG. 3. Plot for the pedestal temperature predicted by Model 2a ($\Delta \propto \sqrt{\rho R q}$) compared with experimental data from 533 data points.
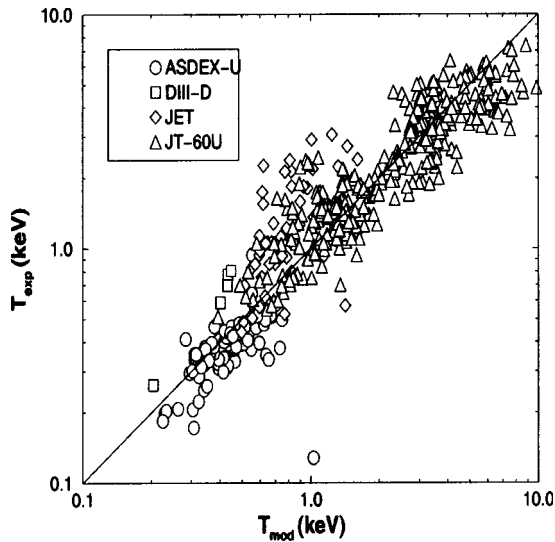
FIG. 4. Plot for the pedestal temperature predicted by Model 3a ($\Delta \propto \rho^{2/3} R^{1/3}$) compared with experimental data from 533 data points.
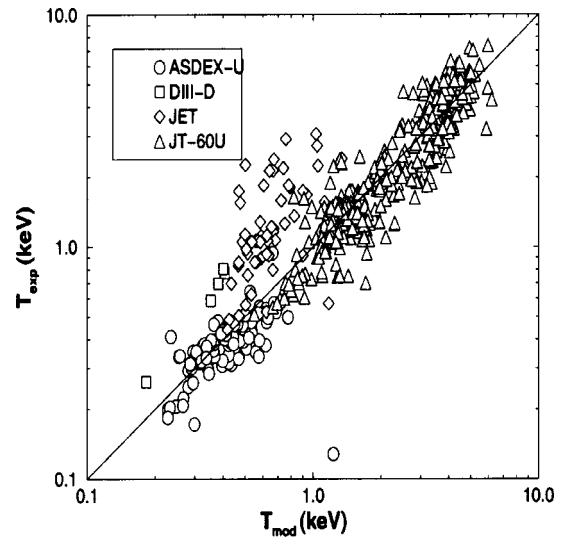
FIG. 6. Plot for the pedestal temperature predicted by Model 5a ($\Delta \propto \epsilon^{1/2} \rho_\theta$) compared with experimental data from 533 data points.

function of n_{ped} and T_{ped}. Consequently, as noted in Sec. IV, Eqs. (13), (17), (19), (24), (27), and (29), combined with Sugihara's shear prescription are nonlinear equations, with T_{ped} appearing on both the left and right sides of the equation.

There are theoretical uncertainties about how much the radial variation in the global magnetic shear really impacts ballooning modes.[22] These uncertainties arise because the ballooning modes can localize in the bad curvature region where the local magnetic shear remains finite even though the global magnetic shear is infinite at the separatrix. Table III summarizes the RMSE of the set of six pedestal width models are used with the simplest prescription of the safety factor and the magnetic shear, as prescription in which the effects of the bootstrap current and the proximity of the separatrix are neglected. For the results shown in Table III, the ballooning stability in the pedestal region is evaluated using

$q = q_{95}$ and a fixed edge magnetic shear $s = 2$ (which is the magnetic shear for a cylindrical plasma with a circular cross section). The RMSEs range from 34.6% to 85.1%. When this simplest magnetic shear model is used, the RMSEs for five of the models are significantly higher than when q and s are calculated as a function of the pedestal width using Sugihara's prescription. However, for Model 2b, the RMSE is only moderately higher. This suggests that a more sophisticated approach than simply setting $q = q_{95}$ and using fixed value of s is required.

We also consider an approach in which the singular nature of the global magnetic shear in the proximity of the separatrix is ignored, but the effects of edge bootstrap current are included, since the edge bootstrap current can lower the edge magnetic shear. With this approach, we use a value of local magnetic shear, $s_0 = 2$, in Eqs. (40) and (41), to compute α_c and use $q = q_{95}$. The RMSE results, which vary
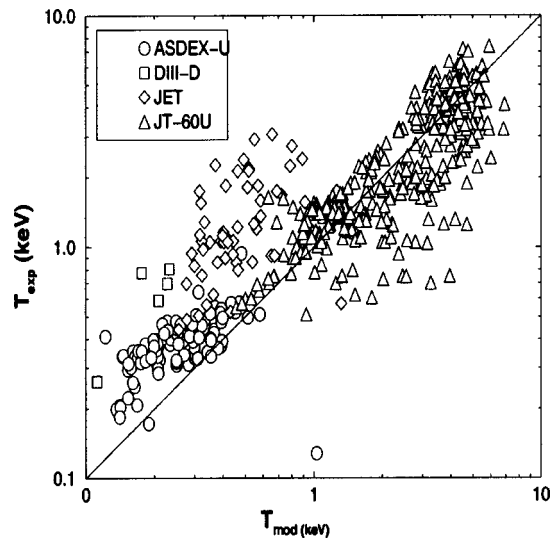
FIG. 5. Plot for the pedestal temperature predicted by Model 4a ($\Delta \propto 1/n_{ped}^{3/2}$) compared with experimental data from 533 data points.
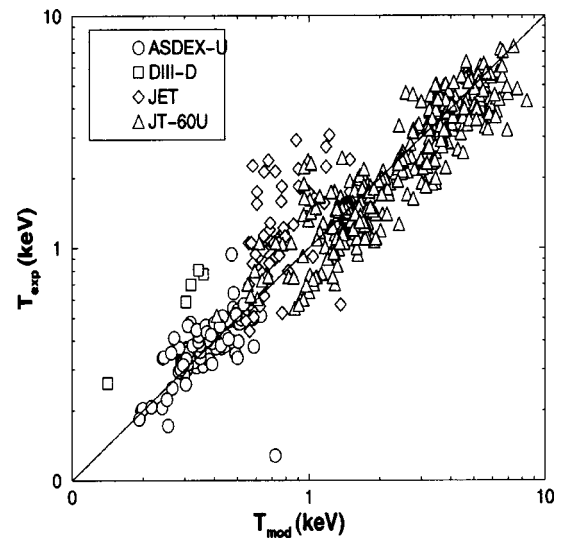
FIG. 7. Plot for the pedestal temperature predicted by Model 6a ($\Delta \propto \sqrt{\beta_\theta} R$) compared with experimental data from 533 data points.

5026   Phys. Plasmas, Vol. 9, No. 12, December 2002

Onjun *et al.*

TABLE III. Coefficient and RMSE of the models using $s=2$ and $q=q_{95}$ for type 1 ELMy H-mode discharges.

Model	Width scaling	C_w	RMSE(%)
1b	$\Delta \propto \rho s^2$	3.98	52.0
2b	$\Delta \propto \sqrt{\rho R q}$	0.26	34.6
3b	$\Delta \propto \rho^{2/3} R^{1/3}$	1.60	40.2
4b	$\Delta \propto 1/n_{\text{ped}}^{3/2}$	4.40	85.1
5b	$\Delta \propto \epsilon^{1/2} \rho_\theta$	3.20	61.6
6b	$\Delta \propto \sqrt{\beta_\theta} R$	0.025	49.3

TABLE IV. Coefficient and RMSE of the models using magnetic shear modified with bootstrap current ($s_0 = 2$) and $q = q_{95}$ for type 1 ELMy H-mode discharges.

Model	Width scaling	C_w	RMSE(%)
1c	$\Delta \propto \rho s^2$	5.16	43.3
2c	$\Delta \propto \sqrt{\rho R q}$	0.29	33.0
3c	$\Delta \propto \rho^{2/3} R^{1/3}$	1.74	37.6
4c	$\Delta \propto 1/n_{\text{ped}}^{3/2}$	4.80	80.7
5c	$\Delta \propto \epsilon^{1/2} \rho_\theta$	3.50	55.8
6c	$\Delta \propto \sqrt{\beta_\theta} R$	0.032	35.9

between 33.0% and 80.7% using this approach, are shown in Table IV. While this approach yields lower values for the RMSE than the results obtained with constant magnetic shear (with no bootstrap current effect) given in Table III, these results do not agree as well with the experimental measurements as those given in Table II, where the bootstrap current and the Sugihara prescription are used. Note that Eqs. (13), (17), (19), (24), (27), and (29) for T_{ped} are nonlinear when the effect of the bootstrap current is included even when the constant s_0 is used.

The results for the pedestal temperature using the Sugihara's shear prescription yields significantly lower RMSE when compared with experimental data, but further work is required to understand the theoretical basis for this prescription. For reasons described above, the ballooning stability might be influenced by the fact that the global magnetic shear is infinite at the separatrix. It may be that there are other factors besides global magnetic shear, such as access to the second stability regime, that are also correlated with distance to separatrix, which could improve the agreement with data. A more detailed numerical study to parameterize the dependence of ballooning stability on various edge parameters (including plasma shape and distance to the separatrix) would be of interest.

There are some simplifications in the model used for the bootstrap current. For example, circular geometry was assumed. Moreover the impact of the bootstrap current on ballooning stability may be more complex than the treatment described in Sec. V. In order to test the effect of these uncertainties, the multiplier C_{bs} that appears in the expression for the bootstrap current, which is used in Eqs. (37), (39)–(41), is varied from its normal value of 1.0. To simplify this analysis, only three models are considered, Model 1c, Model 2c and Model 3c in Table IV, using magnetic shear modified with bootstrap current ($s_0 = 2$) and $q = q_{95}$ (i.e., not using the Sugihara prescription for s and q). The results are summarized in Table V. The best fit to the data is produced when the value of $C_{bs} = 1.5$ is used in Model 1c, in which the pedestal width is based on the magnetic and flow shear stabilization, the value of $C_{bs} = 2.8$ is used in Model 2c, in which the pedestal width is based on the flow shear stabilization, or the value $C_{bs} = 4.1$ is used in Model 3c, in which the pedestal width is based on the diamagnetic stabilization. It should be noted that the RMSE values have relatively broad minima (probably due to the self-limiting nonlinear feedback mechanisms from the bootstrap current in each model). Additional

empirical shaping effects are also investigated by modifying the factor h_s, given in Eq. (40), from the normal value of $h_s = 1.0$. The variation of h_s results in lower values of RMSE, as shown in Table V. Thus, it is shown in Table V that models with empirically determined enhancements of the bootstrap current and shaping effects, but without the Sugihara prescription for the effect of the separatrix on magnetic shear, can produce RMS errors as low as the baseline models with the Sugihara prescription, which were shown in Table II.

In the derivation of the models that yield the pedestal temperature, it is assumed that plasma is in the first stability regime, where the critical pressure gradient is approximately linearly proportional to magnetic shear. A reduction in the magnetic shear will produce a reduction in the normalized pressure gradient α_c. If the bootstrap current is high enough, and the resulting magnetic shear is low enough, the plasma might gain access to the second-stability regime,[23] and under these circumstances the effects of peeling modes and finite n ballooning modes need to be included.[24] Although there is empirical evidence for the importance of the effect of plasma shape on local ballooning limits, as described in Sec. V, there remains uncertainty about the exact strength and functional form of the effects of plasma shape on the ballooning limit. For example, it is not known if elongation and triangularity impact stability directly or if their impact is produced through other effects that are correlated with these parameters. A numerical study to parameterize ballooning stability in terms of a few geometrical parameters would be useful.

Since large numbers of data points are used in this paper from JT-60U and ASDEX-U, the coefficient in the expression for the pedestal width chosen to optimize the RMSE deviation in each of the models will be biased towards optimizing the JT-60U and ASDEX-U data. This might explain why all of the models tend to produce better agreement with the JT-60U and ASDEX-U data than with the DIII-D and JET data. If a fit were carried out with equal weighting for a set of data points from each tokamak, it would result in a model in which the DIII-D and JET data points would lie just above the diagonal line and the JT-60U and ASDEX-U data points would lie just below the diagonal line. In the other words, if the model were calibrated using an equal weight for each data set, the RMS errors for the JT-60U and ASDEX-U data would increase while the RMS errors for the DIII-D and JET data would decrease.

TABLE V. Effect on models 1c, 2c, and 3c of varying the strength of bootstrap current and additional shaping factor, using $s_0 = 2$ and $q = q_{95}$ for type 1 ELMy H-mode discharges.

Model	Width scaling	Bootstrap multiplier C_{bs}	Additional shaping factor h_s	RMSE(%)
1c	$\Delta \propto \rho s^2$	0.0	1	52.0
		1.0	1	43.3
		1.5	1	42.7
		1.5	$\sqrt{(1 + \kappa_{95}^2(1 + 5\delta_{95}^2))}$	42.4
		1.5	$\sqrt{(1 + \kappa_{95}^2(1 + 10\delta_{95}^2))}$	41.2
		1.5	$\sqrt{(1 + \kappa_{95}^2(1 + 20\delta_{95}^2))}$	41.4
2c	$\Delta \propto \sqrt{\rho R q}$	0.0	1	34.6
		1.0	1	33.0
		2.8	1	32.3
		2.8	$\sqrt{(1 + \kappa_{95}^2(1 + 5\delta_{95}^2))}$	31.1
		2.8	$\sqrt{(1 + \kappa_{95}^2(1 + 10\delta_{95}^2))}$	30.5
		2.8	$\sqrt{(1 + \kappa_{95}^2(1 + 20\delta_{95}^2))}$	31.6
3c	$\Delta \propto \rho^{2/3} R^{1/3}$	0.0	1	40.2
		1.0	1	37.6
		4.1	1	35.6
		4.1	$\sqrt{(1 + \kappa_{95}^2(1 + 5\delta_{95}^2))}$	34.8
		4.1	$\sqrt{(1 + \kappa_{95}^2(1 + 10\delta_{95}^2))}$	33.8
		4.1	$\sqrt{(1 + \kappa_{95}^2(1 + 20\delta_{95}^2))}$	34.0

It is clear in Figs. 2–7 that the DIII-D data points always lie farther above the diagonal line than the ASDEX-U data points. This deviation was also observed in the work by Hatae,[11] which was carried out using a less complex pedestal model. This deviation shows that the models in our paper, which include the effect of the bootstrap current and the effect of the separatrix on magnetic shear, do not improve the consistency between the DIII-D and ASDEX-U data. However, this deviation of DIII-D from ASDEX-U data might be explained by access to the second stability regime in the DIII-D plasmas, while the ASDEX-U plasmas are primarily confined to the first regime of ballooning mode stability, as noted by Hatae.[11] The model developed by Hatae and the models in our paper all assume that the pressure gradient is restricted to the first stability regime.

It can also be seen in Figs. 2–7 that the JET data points appear to follow a different trend from the ASDEX-U and JT-60U data points. This deviation was not present in Hatae's results.[11] Hatae found that the JET data points lie roughly along a line parallel to the diagonal line and his model underpredicts the JET pedestal pressure. In contrast our models, which also tend to underpredict the JET pedestal pressure, yield a greater underprediction for discharges with higher pedestal pressure. In Hatae's model, the magnetic shear was taken to be constant, since the magnetic shear was not available for all of the data. The constancy of the magnetic shear in Hatae's model is likely to affect the predictions of the pedestal parameters in the JET discharges. A possible explanation for the underprediction of the JET pedestal temperature is that the JET plasmas might enter the second stability regime, while the ASDEX-U and JT-60U plasmas generally remain in the first stability regime. This idea is supported by the fact that the JET data are influenced by a stronger shaping effect than is the case of the JT-60U and ASDEX-U data, as can be seen in Fig. 8.

B. Statistical uncertainties

There are standard statistical methods for determining whether or not the difference between the RMS errors of two models is statistically significant. These tests are based on certain assumptions about errors being random and uncorrelated. For example, expressing Fisher's z transformation test[25] (used for linear regression) in terms of the RMSE instead of the correlation coefficient, one can show that two models are statistically different at the 95% confidence level if the ratio of their RMS errors, $\mathrm{RMSE}_2 / \mathrm{RMSE}_1$, exceeds approximately $\exp(\sqrt{2/N})$, for a sufficiently large number of data points N. Thus for our case with $N = 533$, all models
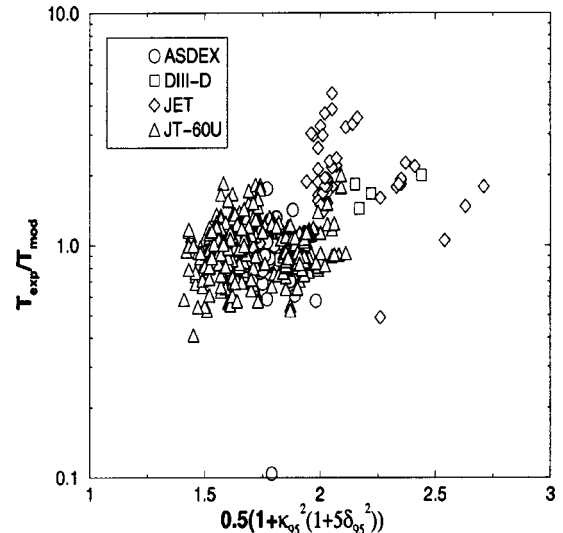
FIG. 8. Plot for the ratio of the experimental temperature to the predicted temperature from Model 5a, with $C_w = 2.57$ and Sugihara's shear prescription, against the value of $0.5(1 + \kappa_{95}^2(1 + 5\delta_{95}^2))$ for type 1 ELMy H-mode data points.

TABLE VI. Average offset and RMS error for individual tokamaks compared with Model 1a and 2a (using Sugihara's shear prescription).

Tokamak	Model 1a		Model 2a	
	Average offset	RMSE(%)	Average offset	RMSE(%)
ASDEX-U	−0.24	35.0	−0.16	31.0
DIII-D	0.32	39.4	0.44	50.5
JET	0.27	48.5	0.37	56.1
JT-60U	0.04	27.7	0.00	24.7

with an RMSE larger than 1.06 times the RMSE of the model with the best fit would appear to be excluded (i.e., all of the models in Table II with an RMSE larger than 32.7% would be excluded). If the assumptions that enter into this are correct, then models 3a, 4a, 5a, and 6a in Table II could be excluded while models 1a and 2a would be statistically indistinguishable. Furthermore, if this statistical approach is correct, it would follow that if these same 4 tokamaks repeated their existing parameter scans to add ten times as much data to the database, we would be able to distinguish between models whose RMSE values differed by only a factor of 1.02.

A problem with this test may be that the assumption that the errors are random and uncorrelated is not valid. It is probable that there are significant systematic errors of various types. While the true pedestal scaling is governed by complicated nonlinear partial differential equations, which represent the detailed physics of the pedestal, we are considering only relatively simple models. In addition, there might be hidden parameters, not yet incorporated in the models, that vary in unknown but systematic ways. For example, some of the tokamaks might systematically operate with different values of plasma–wall separation or collisionality or beam-driven rotation. Various tokamaks use different kinds of wall conditioning and gas fueling methods, and different divertor designs that can change in a single tokamak from year to year. Because of these hidden variables, it is difficult to determine objectively the degree of systematic variation in the data. That is, it is difficult to determine the effective number of independent uncorrelated measurements, N_{eff}, that one can use to set a threshold for distinguishing between the RMS errors produced by the different models.

Visually noticeable evidence of correlated errors can be seen in Figs. 2–7, where it is clear that the JET data are systematically high and have a different trend compared with the scaling. Note that there is only a small number of data points from DIII-D so that it is difficult to see the trend for this tokamak. As shown as an example in Table VI, the JET data have a 27% average offset (0.27 on a log scale) above Model 1a and a 37% average offset above Model 2a, which were the models shown in Table II. This does not necessarily mean that the JET diagnostics for measuring pedestal temperature have a calibration problem that makes them systematically high, or that ASDEX-U has a calibration problem that makes their data systematically low. It very well may mean that we have not yet determined the fully correct model for the pedestal and that JET tends to operate in a different regime (perhaps with higher power, lower collision-

ality, higher shaping, or with a different divertor design). However, it is still useful to re-check the diagnostic methods and fitting techniques used to measure the pedestal temperature on various tokamaks in order to reduce the possibility of systematic errors. For example, the ASDEX-U pedestal measurements in this version of the INTERNATIONAL PEDESTAL DATABASE (version 3.1, the latest public version) are based on measurements at a fixed distance of 2 cm away from the separatrix. This assumption would not be inappropriate if the pedestal width were always less than 2 cm in ASDEX-U. However, models 1a and 2a, for example, predict a pedestal width of approximately 2.0–3.0 cm for ASDEX-U. This issue may be addressed in future versions of the database.

Another example of a possible source of correlated errors is shown in Fig. 8, where $T_{exp}/T_{model5a}$ is plotted as a function of a parameter that measures the strength of the plasma shaping (i.e., elongation and triangularity). This figure shows that there is a large scatter in the ratio of $T_{exp}/T_{model5a}$, especially in highly shaped plasmas. Even though this model (also other models in this paper) already includes a geometrical effect, the geometrical dependence of the model still needs to be improved. Figure 8 also shows that the geometrical factor is systematically different in different tokamaks, which might produce another source of systematic variation between the tokamaks and co-linearity of the data within each tokamak. It can be seen in Fig. 9 that there is more scatter in the ratio $T_{exp}/T_{model5a}$ at high values of the ratio of the pedestal density to the Greenwald density. It can also be seen that JT-60U tends to operate in a lower ratio of density regime than ASDEX-U, DIII-D and JET.

Our work suggests several ways in which additional experiments would yields data that might help to better distinguish between the pedestal models.

C. Useful future experiments

The dependence on plasma shape is important, both because there is evidence of a potentially strong improvement at high triangularity and high elongation,[4] and because the various tokamaks tend to operate with systematic differences in shaping (as shown in Fig. 8). Thus, it would be useful for all tokamaks to scan as large a range of elongation and triangularity as possible. A related question is whether there are any significant differences between H-mode discharges with a single-null divertor and a double-null divertor.

Current ramps would also be a useful way to alter the edge current density and thus edge ballooning stability. This would test key features of the pedestal models. Although,
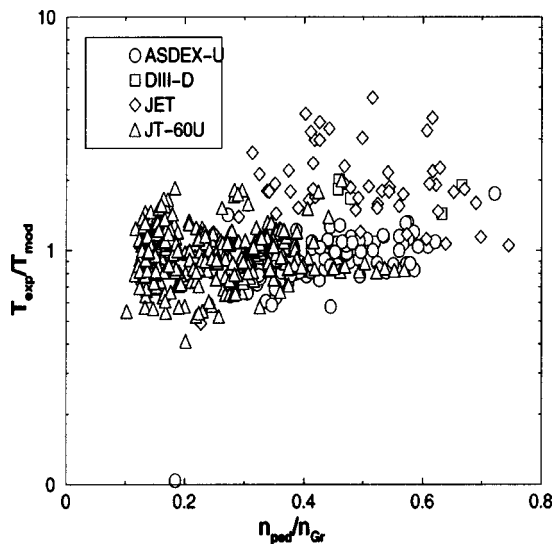
FIG. 9. Plot for the ratio of the experimental temperature to the predicted temperature from Model 5a, with $C_w = 2.57$ and Sugihara's shear prescription against the value of the ratio of the pedestal density to the Greenwald density n_{ped}/n_{Gr} for type 1 ELMy H-mode data points.

current ramp discharges would not be steady state discharges, it would probably not require much of a current ramp to probe this aspect of the models. Hence, the discharges would be close to steady state, at least on the time scale of the pedestal dynamics.

Isotope scans can also help to distinguish between models, since isotope scans provide an independent and direct way to vary the gyro-radius. Previous studies provide some evidence of a strong dependence of the H-mode pedestal height on isotope.[5] This is consistent with a model where the pedestal width varies linearly with the gyro-radius (and a simple expression for the pedestal pressure gradient limit). This isotope scaling is stronger than many of the models in this paper, even stronger than that included in model 1a or model 5a when the Sugihara prescription is used to obtain the results in Table II. Although models 1a and 5a appear to use a pedestal width that scales linearly with the gyro-radius, Sugihara's prescription for computing the magnetic shear at a distance of one pedestal width away from separatrix produces a nonlinear model in which the dependence of the pedestal height on the pedestal width can be much weaker than linear. There are a few data points in the present database from an isotope scan in JET (which included tritium and hydrogen discharges) that suggest the possible existence of a favorable isotope scaling. It is difficult to draw any firm conclusions due to co-linearity, significant scatter in the data, and the small number of discharges in the isotope scan. It would thus be very useful if more tokamaks provided data of hydrogen and deuterium discharges with a wide range of plasma shapes and plasma conditions.

Finally, it would also be useful to expand the range of densities in the database, since the difference between the extremes of pedestal scalings $\Delta \propto \rho_\theta$ and $\Delta \propto R\sqrt{\beta_{ped,\theta}}$ is approximately a factor of only $R\sqrt{n/A_H}$. At present, n_{ped}/n_{Gr} (where n_{Gr} is the Greenwald density defined in Table I) varies from about 0.1 to about 0.75, with only 19 data points

(out of 533) near the upper end of this range, $0.6 < n_{ped}/n_{Gr} < 0.75$. There is experimental evidence of degraded performance at high density (though this can be offset at high triangularity). It would be useful to know whether the present pedestal scalings continue to hold at even higher densities.

VII. CONCLUSIONS

A range of models are developed for predicting temperature at the top of the pedestal which occurs at the edge of H-mode plasma in tokamaks. The results for the pedestal temperature obtained are compared with 533 experimental data points with type 1 ELMs in the International Pedestal Database.[11] These models are based on six theory-motivated scalings for the width of the pedestal. We have also explored several approaches to calculate the magnetic shear and the safety factor, quantities which enter the criteria for the ballooning mode stability assumed to yield the critical pressure gradient In one approach for calculating the magnetic shear and safety factor, a prescription includes the variation of the global magnetic shear with radius This prescription, the Sugihara prescription, yields the best agreement with the data in the International Pedestal Database. Excluding the pedestal model based on the width that scales as the neutral penetration length, the various models have comparable RMSEs in the range of 30.8%–34.4%. It is difficult to distinguish between a number of the different models, in part because of the co-linearity in the data and because of systematic differences between tokamaks.

ACKNOWLEDGMENTS

[1] Y. Kamada, O. N. K. Ushigusa et al., Plasma Phys. Controlled Fusion **36**, A123 (1994).
[2] T. Hatae, Y. Kamada, S. Ishida et al., Plasma Phys. Controlled Fusion **40**, 1073 (1998).
[3] Y. Koide and the JT-60U Team, Phys. Plasmas **4**, 1623 (1997).
[4] Y. Kamada, R. Yoshida, K. Ushigusa et al., Proceedings of the 16th IAEA Fusion Energy Conference, Montreal, 1996, Vol. 1, p. 79.
[5] The JET Team (presented by J. G. Cordey), in Proceedings of the Seventeenth International Atomic Energy Agency Fusion Energy Conference, Yokahama, Japan, 19–24 October 1998 (International Atomic Energy Agency, Vienna, 1999), paper IAEA-F1-CN-69/EX7/1.
[6] J. Lingertat, V. Bhatnagar, G. D. Conway et al., J. Nucl. Mater. **266–269**, 124 (1999).
[7] T. H. Osborne, K. H. Burrell, R. J. Groebner, L. L. Lao, A. W. Leonard, R. Maingi, R. L. Miller, G. D. Porter, G. M. Staebler, and A. D. Turnbull, J. Nucl. Mater. **266–269**, 131 (1999).
[8] T. H. Osborne, R. J. Groebner, L. L. Lao et al., Plasma Phys. Controlled Fusion **40**, 131 (1998).

[9] M. Sugihara, Y. Igitkhanov, G. Janeschitz *et al.*, Nucl. Fusion **40**, 1743 (2000).

[10] J. Connor, Plasma Phys. Controlled Fusion **40**, 191 (1998).

[11] T. Hatae, M. Sugihara, A. E. Hubbard *et al.*, Nucl. Fusion **41**, 285 (2001).

[12] I. Hutchinson, R. Boivin, F. Bombarda, P. Bonoli, S. Fairfax, J. G. C. Fiore, S. Golovato, R. Granetz, M. Greenwald, S. Horne *et al.*, Phys. Plasmas **1**, 1511 (1994).

[13] O. Gruber *et al.*, Nucl. Fusion **39**, 1321 (1999).

[14] J. L. Luxon and L. G. Davis, Fusion Technol. **8**, 441 (1985).

[15] P. H. Rebut, R. J. Bickerton, and B. E. Keen, Nucl. Fusion **25**, 1011 (1985).

[16] M. Mori, S. Ishida, T. Ando *et al.*, Nucl. Fusion **34**, 1045 (1994).

[17] B. N. Rogers and J. F. Drake, Phys. Plasmas **6**, 2797 (1999).

[18] K. C. Shaing, Phys. Fluids B **4**, 290 (1992).

[19] D. P. Stotler, W. T. Reiersen, and G. Bateman, Comput. Phys. Commun. **81**, 261 (1994).

[20] J. Wesson, *Tokamaks* (Clarendon, Oxford, England, 1997).

[21] G. W. Hammett, W. Dorland, M. A. Beer, and M. Kotschenreuther, *Proceedings of the Workshop on Opportunities and Directions in Fusion Energy Science for the Next Decade*, Snowmass, CO, July 1999 (www.pppl.gov/snowmass/details.html).

[22] C. M. Bishop, R. Kirby, J. W. Connor *et al.*, Nucl. Fusion **24**, 1579 (1984).

[23] R. L. Miller, Y. R. Lin-Liu, T. H. Osborne, and T. S. Taylor, Plasma Phys. Controlled Fusion **40**, 753 (1998).

[24] H. R. Wilson, J. W. Connor, A. R. Field *et al.*, Phys. Plasmas **6**, 1925 (1999).

[25] M. R. Spiegel, *Statistics* (McGraw-Hill, New York, 1961).